Laterally coupled vertical-cavity surface-emitting lasers with tunable resonance width and frequency

Original
Laterally coupled vertical-cavity surface-emitting lasers with tunable resonance width and frequency / Lindemann, M., D'Alessandro, M., Ledentsov, N., Makarov, O.Y., Ledentsov, N.N., Tibaldi, A., Gerhardt, N.C., Hofmann, M.R.. - In: JOURNAL OF APPLIED PHYSICS. - ISSN 1089-7550. - STAMPA. - 138:5(2025), pp. 1-12. [10.1063/5.0275622]

Publisher:
AIP publishing

Published
DOI:10.1063/5.0275622

Journal of
Applied Physics

RESEARCH ARTICLE | AUGUST 01 2025

Laterally coupled vertical-cavity surface-emitting lasers with tunable resonance width and frequency

M. Lindemann ✉ ; M. D'Alessandro ; N. Ledentsov, Jr. ; O. Y. Makarov; N. N. Ledentsov ;
A. Tibaldi ; N. C. Gerhardt ; M. R. Hofmann

J. Appl. Phys. 138, 053102 (2025)
https://doi.org/10.1063/5.0275622

Articles You May Be Interested In

Chirped arrays of diode lasers for supermode control

Appl. Phys. Lett. (August 1984)

Supermodes of multiple-stripe quantum-well heterostructure laser diodes operated (cw, 300 K) in an external-grating cavity

J. Appl. Phys. (March 1985)

Controlled fundamental supermode operation of phase-locked arrays of gain-guided diode lasers

Appl. Phys. Lett. (September 1984)

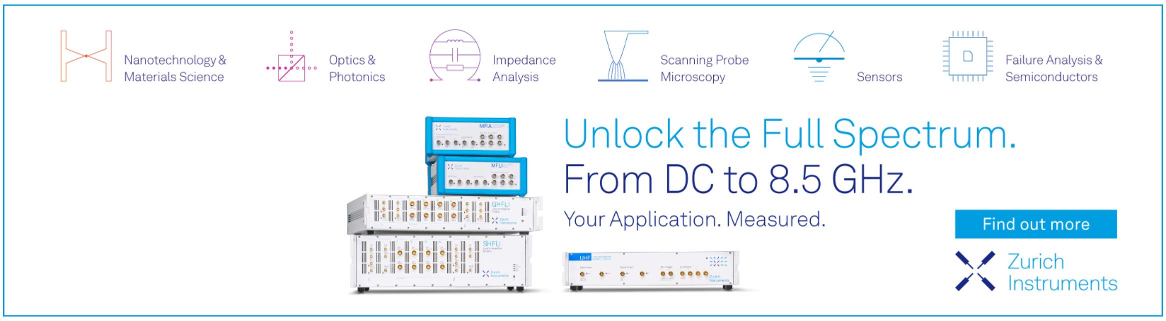

AIP Publishing

Journal of
Applied Physics

ARTICLE

pubs.aip.org/aip/jap

Laterally coupled vertical-cavity surface-emitting lasers with tunable resonance width and frequency

Cite as: J. Appl. Phys. **138**, 053102 (2025); doi: 10.1063/5.0275622
Submitted: 14 April 2025 · Accepted: 7 July 2025 ·
Published Online: 1 August 2025

View Online Export Citation CrossMark

M. Lindemann,[1,a)] M. D'Alessandro,[2] N. Ledentsov, Jr.,[3] O. Y. Makarov,[3] N. N. Ledentsov,[3] A. Tibaldi,[2] N. C. Gerhardt,[1] and M. R. Hofmann[1]

AFFILIATIONS

[1] Photonics and Terahertz Technology, Ruhr-Universität Bochum, 44801 Bochum, Germany
[2] Department of Electronics and Telecommunications, Politecnico di Torino, 10129 Turin, Italy
[3] VI-Systems GmbH, 10623 Berlin, Germany

[a)] **Author to whom correspondence should be addressed:** markus.lindemann@rub.de

ABSTRACT

Laterally coupled vertical-cavity surface-emitting lasers (VCSELs) can exhibit additional resonances at high modulation frequencies that can substantially increase the laser's modulation bandwidth. State-of-the-art laterally coupled devices require non-standard manufacturing technology and precise tuning of the currents supplied to each cavity separately to form optical supermodes suitable for such resonances. Here, we report on a novel switching phenomenon in laterally coupled VCSEL structures having only a single common electric contact and manufactured in a standard oxide-confined VCSEL geometry. At lower currents, they can be operated in a weakly coupled (WCR) regime and, at higher currents, in an injection-locked (IL) regime, enabling fundamentally different spectral and dynamic features. In the WCR, both optical supermodes lase and a narrow tunable plasma-assisted peak at their beating frequency is observed for each of the apertures, with a current-dependent frequency tuning and anti-phase intensity oscillations in each of the cavities. In contrast, in the IL regimes, only one (anti-symmetric) supermode lases. This adds a broader resonance to the modulation response while the intensity oscillations in both cavities are in-phase. Only the IL regime can result in increased modulation bandwidth of the system. Measurements of the pulse responses and continuous modulation up to 70 GHz for both operational regimes are presented and compared with simulations of our distributed rate equation model whose parameters are extracted from full-wave electromagnetic simulations of the device, including the temperature distribution in the device. Excellent agreement is found and enables comprehensive understanding of the dynamics of supermodes in oxide-confined coupled cavity VCSELs.

I. INTRODUCTION

The demand for high modulation speeds in optical data transmission continues to grow.[1,2] For short-haul links, e.g., in data-centers, vertical-cavity surface-emitting lasers (VCSELs) are commonly used for direct current modulation schemes, making them an important component of the networking infrastructure. The modulation bandwidth of conventional VCSEL devices remains constrained by the relaxation oscillation frequency (ROF), which is determined by the intrinsic photon-carrier resonance of the device. The ROF scales with the square root of the current density, thus higher ROF values require larger current densities leading to high energy consumption, potentially also resulting in overheating that limits both ROF and device reliability. Therefore, alternative strategies to enhance the modulation speed of VCSELs using direct current modulation need to be developed.

Proposed approaches include integration of an electro-optic modulator to bypass the intrinsic ROF of the semiconductor laser, yielding in demonstration of at least 35 GHz modulation bandwidth,[3,4] or utilizing lateral photonic crystal structures to increase the differential gain allowing for high data rates at very low current densities.[5] Also, replacing the carrier dynamics by spin and polarization dynamics was demonstrated to achieve modulation frequencies exceeding 200 GHz.[6] An alternative strategy involves incorporating additional resonances into the modulation bandwidth by designing transversely coupled-cavity (TCC) resonators.[7–9] The latter have been developed and demonstrated by several groups, including bowtie devices,[8] vertically coupled and photonic-crystal VCSELs,[10–12] double-transverse-coupled-cavity VCSELs[13] and daisy-like VCSELs.[14] A design of a 980 nm VCSEL laterally coupled to six hexagonal feedback cavities enabled a substantial increase in modulation bandwidth, achieving a -3 dB bandwidth exceeding 45 GHz (limited by the experimental setup).[14] A significant improvement in modulation bandwidth and data transmission at 30 Gbit/s could also be demonstrated.[15]

All these approaches, however, require non-standard VCSEL technology, such as photonic-crystal manufacturing,[12] proton implantation[8] for electrical separation of the two cavities, or complicated contacting.[14] In addition, bandwidth enhancement requires critical tuning of both currents and geometrical parameters. In North *et al.*,[12] it is shown how the coherent coupling of two apertures defined in a photonic crystal structure is obtained only for a precise set of injection currents in the two cavities. In Dalir and Koyama[8] instead, the resonance is controlled by a tuning of the current injected in the passive cavity.

In this study, we demonstrate for the first time the coherent operation of a 2 × 1 aperture TCC-VCSEL, requiring only a single contact and with a simple standard oxide-confined VCSEL fabrication process. This advancement enables a more cost-effective and easy-to-use technology, expanding the potential of TCCs for industrial applications.

We provide a detailed characterization of the two static regimes the device can operate: The first one, referred to as weakly coupled regime (WCR) is found at low bias current, featuring two lasing supermodes and different dominant wavelengths in each cavity. This leads to an oscillation of the photon densities, which couples to the carrier plasma, resulting in a continuously generated plasma-assisted beating (PAB) adding a narrow PAB peak to the intensity modulation response (IMR). The second one, referred to as monolithic self-injection locking (SIL), instead features a single lasing supermode and a coherent, phase-coupled operation of the two apertures. We show how this second regime can lead to an enhancement of the intensity modulation response by an additional photon–photon resonance (PPR) and how it is easily observed by increasing the bias current. This may be explained by a combination of device geometry, self-heating effects, and carrier dynamics effects, that will be analyzed both experimentally and theoretically.

While TCC-VCSELs are primarily intended for high-speed data transmission within the self-injection locked range, this study also highlights additional promising applications of the WCR: First, Radio-over-Fiber is an important application of current and future energy- and cost-effective wireless networking.[16] Radio-over-Fiber requires a light source that features modulation at RF-carrier frequencies. For this purpose, the PAB of the supermodes in the weakly coupled regime can be used, while additional signals can be added using direct modulation. Dispersion limitations of fiber systems can be avoided by the narrow laser line width, while increased optical power is supplied by the array configuration, making the coupled-cavity VCSELs good candidates for optical sources in Radio-over-Fiber systems.[17]

Generation of radiation in the terahertz range is another topic of current research interest, which can be addressed operating this laser type in the WCR. The standard approach to generate continuous wave terahertz radiation is to tune two single mode lasers to the desired frequency spacing of 0.1 THz and more. Two tunable lasers are however bulky and require exact alignment for beam overlapping. In contrast, the modes in the investigated TCC-VCSELs shift with different rates over current, such that an extremely compact tunable two color laser source can be obtained. We demonstrated already that the TCC-VCSELs can be used to generate THz radiation with a tuning range of several hundred GHz.[18] Furthermore, the devices can be utilized for beam steering[19,20] and possibly other applications yet to be explored.

To investigate SIL and WCR, in this work the devices in our study are (I) characterized steady state by spectrally resolved beam shape analysis, (II) spectrally characterized with a high-resolution optical spectrum analyzer, (III) electrically modulated up to 70 GHz, (IV) operated under ultrashort pulse injection. For (III) and (IV), the output is analyzed with a streak camera with spatial and spectral resolution, enabling insights in the dynamics with modal resolution and with respect to each cavity separately. The operational ranges of WCR and SIL are analyzed using techniques (I)–(IV).

Phase coupled operation in TCC-laser arrays has been extensively studied in the literature by means of coupled mode theory,[21,22] also including the effect of a non-uniform gain distribution.[23] More recently, concepts from parity-time symmetry and exceptional points[24] were introduced to describe the physics of TCC-VCSELs. In this context, Gao *et al.*[25] provide an experimental and theoretical demonstration of mode hopping and beam steering in a 2 × 1 photonic crystal VCSEL array.

Our proposed modeling approach is based on the solution of the scalar wave equation, carried out by an expansion of the electric field as a sum of the cavity (super)-modes[26] and coupled to the carrier diffusion problem. In contrast to the previous works, we self-consistently solve the dynamics of carriers and electric field, introducing the possibility of simulating dynamical effects, such as the pulse excitation,[27] dynamical stability[28] properties and the IMR, including the effects of spatially dependent probing.[26] We especially focus on the transition between the WCR and SIL regime, providing both spatial and spectral analysis for static and dynamic investigations.

This work is structured as follows. First, we will give details on the sample used, followed by a description of how the laser device is modeled for the simulations. We continue with a presentation of the results of experiments (I)–(IV) and a comprehensive analysis of the results based on comparison with simulated data.

II. DEVICE

Our mini-array VCSEL design is remarkably simple and completely based on standard manufacturing steps, which is beneficial for manufacturing complexity and device costs. Our devices utilize conventional oxide-confined apertures to enable controlled coupling between the cavities. Furthermore, in our samples all apertures have common p- and n-contacts. The devices can be designed to operate in a stable single mode regime up to high currents. For small aperture-to-aperture pitch sizes of less than around 11 μm, optical leakage-induced interaction between apertures gets strong enough to allow coherent lasing of all apertures. In our devices, the SIL or coherently coupled current range is significantly large and covers several mA.

The device is mounted and bondwired on a V-connector, enabling high-frequency electrical modulation. It is operated in a room-temperature environment without additional temperature controller.

The device investigated is a 2×1 coupled cavity VCSEL of which Fig. 1(a) shows a microscope image. The oxide aperture can be seen revealing the two apertures AP1,2 being connected with a bridge of 1.2 μm diameter, while AP1,2 having a spacing of only 5 μm. The apertures share a common electrical contact. In a previous publication,[26] we have described how we model the dynamics of the device by using a lumped rate equation that is parameterized based on the results of a vectorial electromagnetic solver for a perfectly symmetrical structure. In Sec. III, we extend the analysis to include thermal effects, structural asymmetries, and a more quantitative analysis of the spatial hole burning, adopting a distributed model for the carrier diffusion problem.

III. MODELING

We numerically solve the scalar wave equation together with the carrier diffusion problem. A dynamic rate equation for the complex electric field amplitude is achieved by representing the electric field phasor as a superposition of the modes with no excitation (”cold cavity”) and by applying the slowly varying approximation[26]

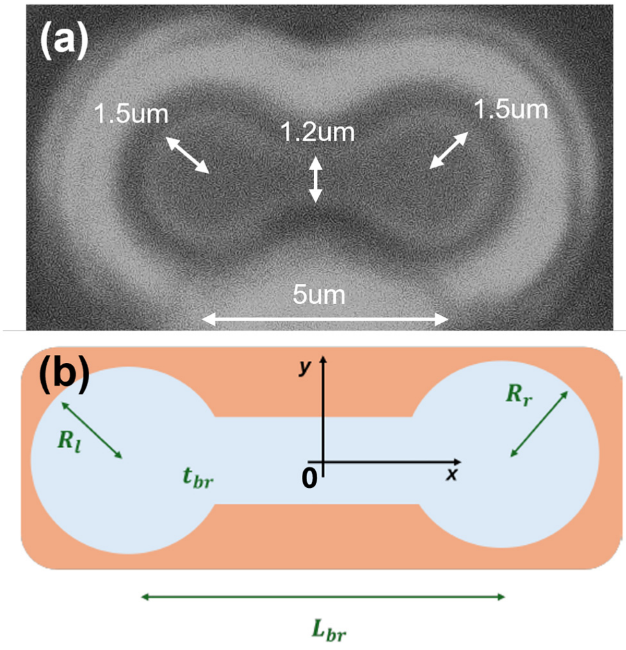

FIG. 1. Photography of the two aperture (AP1, AP2) device used in this study (a). Sketch of the oxide aperture, consisting of two circular apertures with radius $R_{l,r}$, linked by a central region called *bridge*, with thickness t_{br} (b). The bridge length L_{br} is defined as the distance between the centers of the two apertures.

$$\partial_t E_i = \left(-\frac{1}{2\tau_{pi}} + i\omega_i\right)E_i + \sum_j k_{ij}E_j. \tag{1}$$

Here, E_i is the complex amplitude of the ith mode, τ_{pi} is the ith mode's photon lifetime, ω_i is the ith frequency separation with respect to the first mode. The terms k_{ij} are derived in Ref. 26 and are

$$k_{ij} = (1 + i\alpha_{\text{h}})\Gamma_z v_{\text{g}} \iint_{AR} \Psi_i g(x, y, t)\Psi_j^* dxdy, \tag{2}$$

where Ψ_i is the modal envelope of the ith mode AR denotes the active region, Γ_z is the longitudinal confinement factor, v_g is the group velocity in the AR, α_h is the linewidth enhancement factor, g is the material gain, computed as

$$g = \frac{G_{\text{d}}(N(x, y, t) - N_0)}{1 + \epsilon S(x, y, t)}, \tag{3}$$

where N_0 is the transparency carrier density, G_d is the active region differential gain, ϵ is the non-linear gain compression factor, and S is the photon density. In this work, we adopted a simplified gain model, neglecting any spectral dependence. This is a reasonable approximation, especially for the first two frequency-close modes, and it is sufficient to describe the observed experimental evidence. The photon density is computed as the absolute value squared of the electric field,

$$S = \left|\sum_i E_i \Psi_i(x, y)\right|^2. \tag{4}$$

Finally, N is the carrier density per unit volume averaged in the AR, which is a solution of the carrier diffusion problem,

$$\partial_t N = -\frac{N}{\tau_{\text{N}}} - v_{\text{g}} g S + D_{\text{n}} \nabla^2 N + \frac{J(x, y, t)}{qW}, \tag{5}$$

where τ_N is the carrier lifetime related to nonradiative recombinations, D_n is the diffusivity, W is the active region width, q is the electron charge, and J is the current density injection profile.

The first step required for evaluating the set of equations derived so far is the computation of the electromagnetic modes, together with their emission frequency and photon lifetime. For this purpose, we use an in-house electromagnetic solver based on coupled mode theory.[29] The modes are determined under the assumption of linear polarization (LP modes), as it is a good approximation for circular oxide apertures.[30] This approach involves a dominant transverse component along the x or y polarization, with a negligible z component. The simulated structure replicates the manufactured one, including the oxide aperture illustrated in Fig. 1. In particular, $R_{\text{l,r}}$ is the radius of the left and

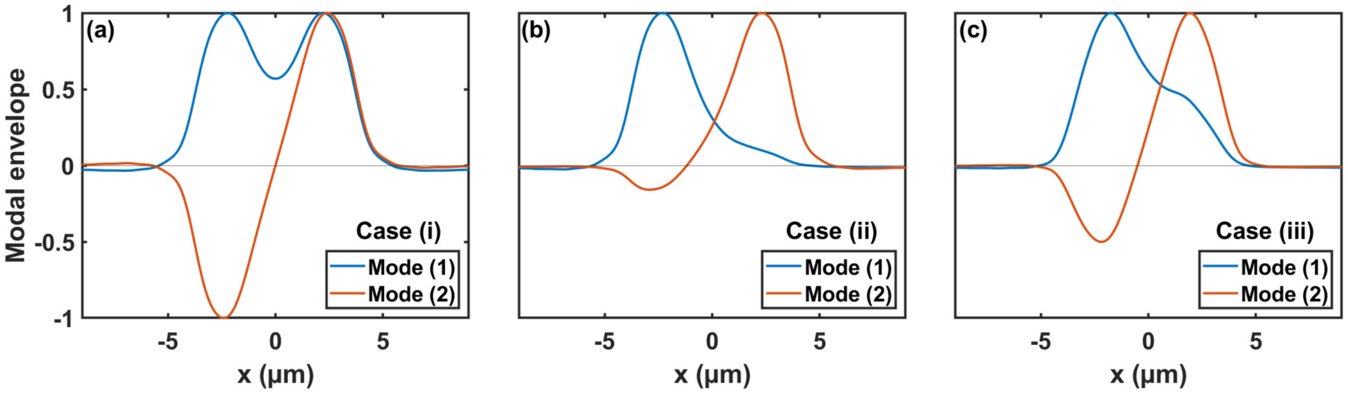

FIG. 2. Cuts of the modal envelopes of the first two modes at $y = 0$. Case (i): symmetric structure (a), case (ii): asymmetric structure (b), case (iii): asymmetric structure with thermal profile (c).

right apertures, while t_{br} and L_{br} are the width and the length of the bridge. In Fig. 2, we report the first two computed electromagnetic modes together with their emission frequency separation for three cases (we number the modes for increasing emission frequency):

(i) symmetric structure, with $R_{\mathrm{l,r}} = 1.5\,\mu\mathrm{m}$ without self-heating effects,
(ii) asymmetric structure, with $R_{\mathrm{l}} = 1.5\,\mu\mathrm{m}$ $R_{\mathrm{r}} = 1.4\,\mu\mathrm{m}$ without self-heating effects,
(iii) asymmetric structure, with $R_{\mathrm{l}} = 1.5\,\mu\mathrm{m}$ $R_{\mathrm{r}} = 1.4\,\mu\mathrm{m}$ with accounted self-heating effects.

For all the three cases, $L_{\mathrm{br}} = 5\,\mu\mathrm{m}$, $t_{\mathrm{br}} = 1.1\,\mu\mathrm{m}$. The thermal profile has been assumed as

$$T(x, y) = T_0 + T_{\mathrm{offset}} e(x, y), \tag{6}$$

where T_0 is the room temperature and $T_{\mathrm{offset}} = 30\,\mathrm{K}$, $e(x,y)$ is a function whose level curves are elliptical, fitted to thermal diffusion simulations. The effect of temperature is accounted with a variation of the refractive index via a phenomenological linear relation $\delta n/\delta T$. The material parameters used for the dynamical and electromagnetic simulations are given in Table I, while the resulting modal parameters are given in Table II.

TABLE I. Material parameters.

Parameter	Value	Unit
W	6.5×4	nm
α_h	2	…
ϵ	3×10^{-23}	m^3
τ_N	1	ns
G_d	1×10^{-19}	m^2
N_0	2.2×10^{22}	m^{-3}
$\delta n/\delta T$	2.2×10^{-4}	K^{-1}

The modal envelopes fundamentally agree with the early theoretical supermode works.[21–23] The symmetric structure (i) supports two (one even and one odd) supermodes (i.e., modes localized in both cavities). In D'Alessandro *et al.*,[26] it has been shown how this configuration can lead to a bandwidth enhancement if only one of the two supermodes is lasing. In the asymmetric case (ii), it can be seen how the two optical modes are instead almost completely localized separately in the two cavities, hence almost non-interacting. Case (iii) shows the effect of temperature, which is threefold: the modes become less localized, hence tending to case (i), the frequency separation increases, as observed in Ledentsov *et al.*[31] and modes experience a lensing toward the center of the structure.

The analysis of Fig. 2 suggests a complex interplay between the unwanted symmetry breaking, which tends to decouple the modes in the two cavities and the thermal lensing, which has the opposite effect.

The third and fourth modes are included in the dynamical analysis but not shown in Fig. 2 for conciseness. As general comments, their modal envelopes are not significantly varying with the temperature. More details about the modal features are reported in Table II.

TABLE II. Modal parameters at temperature offset $T_{\mathrm{offset}} = 30\,\mathrm{K}$ from room temperature.

Parameter	Value	Unit
$\tau_{p,1}$	2.01	ps
$\tau_{p,2}$	2.08	ps
$\tau_{p,3}$	2.04	ps
$\tau_{p,4}$	2.01	ps
f_1	0	GHz
f_2	41	GHz
f_3	332	GHz
f_4	661	GHz
Γ_z	0.33	…

IV. STATIC OPERATION

Once the modes are computed, the transition from the WCR to SIL regime can be investigated by solving Eqs. (1)–(5). The carrier diffusion equation is discretized using a finite element modeling (FEM) method on a mesh generated by the software Gmesh[32] and solved with ode45 of Matlab.[33] The current density injection profile $J(x, y)$ is set uniform on the oxide aperture. We report the case of injected current 7.5 mA and 8 mA, keeping the temperature offset of $T_{\text{offset}} = 30\,\text{K}$ from room temperature. In the former case, the system is in WCR, that means the solution can be expressed in the form

$$E(x, y, t) = \Psi_1 A_1 e^{i\tilde{\omega}_1 t} + \Psi_2 A_2 e^{i\tilde{\omega}_2 t} + \cdots, \tag{7}$$

where $\tilde{\omega}_i$ and A_i are the frequency offsets and complex amplitudes, both solutions of the dynamical problem. The amplitudes A_i for sake of understanding can be considered as constant plus small oscillating components.

In the second case instead, the system is in SIL that means the solution can be expressed as

$$E(x, y, t) = (\Psi_1 A_1 + \Psi_2 A_2) e^{i\tilde{\omega}_{12} t} + \cdots, \tag{8}$$

where $\tilde{\omega}_{12}$ is an intermediate frequency which has to be found as a solution of the dynamical problem. It is important to notice that the first two modes are in phase locking,[23] meaning that they oscillate at the same frequency $\tilde{\omega}_{12}$.

For a better visualization of Eqs. (8)–(7), the Fourier transform of the sum of the modal amplitudes is reported in Fig. 3 for the two currents. It can be seen how a peak is present for each mode, plus smaller peaks linked to second harmonic in WCR. The insets show the modal envelope corresponding to the lines of the third and fourth modes.

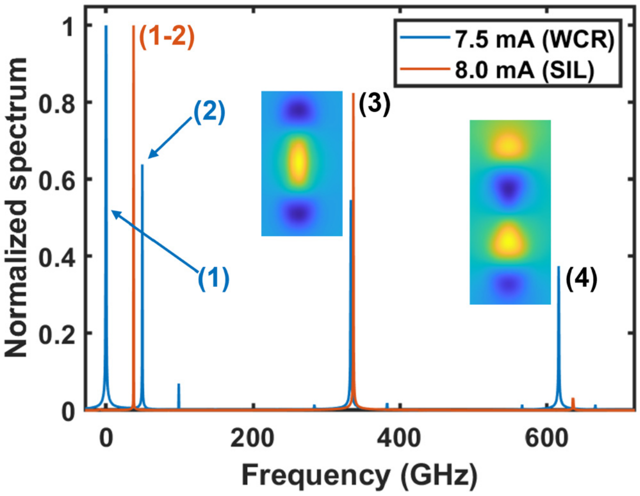

FIG. 3. Simulated optical spectra for WCR (7.5 mA) and SIL (8.0 mA) regimes. It can be seen how the lines corresponding to the first two modes merge into a single one after the transition to SIL. The insets show the modal envelope corresponding to the 3rd and 4th modes spectral lines, which is the same in SIL and WCR case.

For better understanding the transition from WCR to SIL, the frequency resolved near field (FRNF) is computed as

$$NF(f, x) = \left| \sum_{i=1:4} A_i(f) \Psi_i(x, 0) \right|,^2 \tag{9}$$

where $\Psi_i(x, 0)$ is a cut of the ith mode at $y = 0$ (like the ones reported in Fig. 2) and $A_i(f)$ is the Fourier transform of the ith modal amplitude. A numerical broadening has been added to mimic the resolution of the measurement setup. In Fig. 4, the FRNF is reported for the two regimes. Inspecting frequency and space at the same time suggests that in WCR each cavity features a predominant frequency, as suggested in Ref. 31, while in SIL, the two cavities are coherently emitting. It can be seen that the NF appears to be an odd configuration, visible from the *zero* at the center of the bridge, in accordance with experiments.

This latter aspect explains why the transition from WCR to SIL advantages the third mode, which is more present in the center, and penalize the fourth one.

The transition to SIL can be therefore interpreted as a phase locking of the two close frequency modes. The conditions for a stable SIL are a complex topic that deserves to be analyzed into details in future works. As a general comment, the SIL solution is possible only for some frequency ranges, in the order of tens of GHz, in agreement with the standard theory of injection locking.[34] Also, the modal overlap plays a major role, due to the coupling coefficients k_{ij}. This latter effect is strongly influenced by the temperature in the analyzed structure. Material and modal parameters, such as α_H and the threshold gain separation also play an important role that will be studied in detail in future works. Figure 5 shows an x-cut of the normalized gain profile, for I = 7.5 (WCR) and 8 mA (SIL). It can be seen that the gain profile significantly changes in the two regimes, due to the different distribution of the photon densities. This results in a change in the eigenvalues of the coupling matrix k_{ij}, which provide the resonant frequencies of the device.[25] Therefore, this change of regime can result in changes

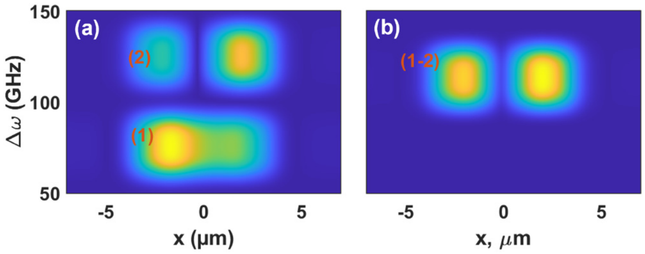

FIG. 4. Simulated frequency and space resolved near field including self-heating effects, i.e., case (iii). Detail of the first two modes reported at 7.5 mA, WCR (a) and 8.0 mA, SIL (b).

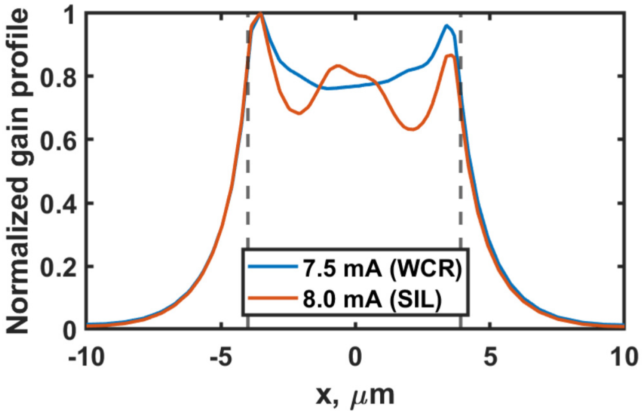

FIG. 5. x-cut of the normalized gain distribution for at 7.5 mA (WCR) and 8.0 mA (SIL), computed from the carrier density with Eq. (3). The dashed lines denote the injection window.

in the frequency separations, observed as a frequency *jump* in the IMR.

We now proceed with the experimental investigation of the near field of both apertures. In agreement with the simulations, we are able to use the beam profile to distinguish between the WCR case, in which the two supermodes are lasing, and the SIL range, in which only one supermode is lasing. The near field is shown in Fig. 6(a) for the WCR case and in Fig. 6(b) for the SIL case. The horizontal axis of the plots corresponds to the array axis position, while the vertical axis corresponds to a spectral resolution. The image was acquired through a microscope. Between the objective lens of the microscope and the CCD camera, a 750 nm blazed diffraction grating was placed. The grating allowed to separate the image into wavelengths along one axis.[35]

It can be observed that the two apertures in Fig. 6(a) have slightly differing emission wavelengths, corresponding to asymmetric supermode localization, as expected from the modal analysis and indicated in the inset of Fig. 4(a). In contrast, for the SIL case it is observed that the emission wavelengths of both apertures do not differ within the range of measurement accuracy, which indicates coupled supermodes, as well expected from the modal analysis and indicated in the inset of Fig. 4(b). Furthermore it is evident that zero intensity is located in the center, which indicates out-of-phase coherent operation.[36]

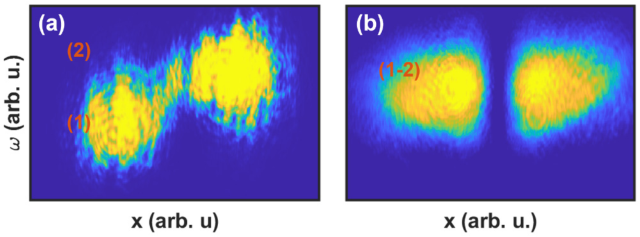

FIG. 6. Measured near field showing the fundamental supermodes in the WCR regime (a) and in the SIL regime (b).

For further analysis, we show the far-field (FF) for the WCR and SIL cases [Fig. 7(a) and 7(b)] as well as the spectra of the two cases in Fig. 7(c). The FF images as well as the spectra reveal that there are higher order modes, while the difference between the two operational regimes can be clearly observed: In FF zero intensity between the two maxima is found in SIL case only, and the spectra demonstrate the evolution from two spectral peaks of the fundamental supermodes in WCR to a single peak in SIL, as expected by theory and shown in Fig. 7. The spectrum for the SIL case in Fig. 7(c) has been shifted for 291.1 GHz to compensate for the redshift due to the increased current. The shift amount is defined by overlapping the peak of mode (3), as it is known from previous studies that the frequency distance between the lowest frequency peak and (3) remains low in the range of a few GHz for a current increase of 1 mA.

V. PULSE RESPONSE

We continue our study with pulse response analysis. The advantage of pulse response analysis is that it allows to measure resonance frequencies only limited by the used streak camera time resolution. The used streak camera can resolve oscillations

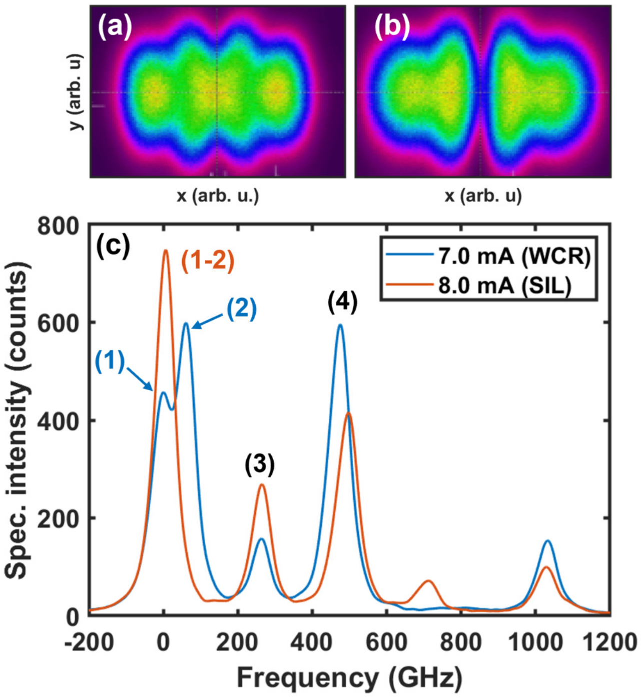

FIG. 7. Far-field in the WCR regime (a) and in the SIL regime (b). Measured spectra in the WCR (7mA) and SIL (8mA) (c). Traces have been shifted to compensate for the heating-induced redshift for enabling comparison.

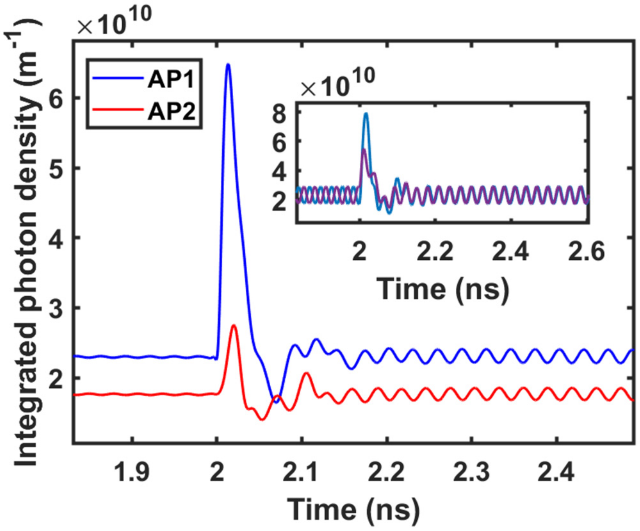

FIG. 8. Simulated streak camera response at 2 mA, in WCR. The average on 100 samples of the photon densities are integrated on the left (red trace) and right (blue trace) cavities and reported as a function of time. It can be seen that the PAB oscillations are in anti-phase in the two cavities. Top right inset: example of left trace for two different samples. Their phase is random before the pulse and aligned after it.

>300 GHz depending on the time range settings, which is much more than direct electrical modulation can supply.

We begin with the simulation of the pulse excitation in combination with this streak camera experiment. To imitate its triggered principle of operation, we average the result of 100 simulations with random initial conditions (i.e., before the trigger occurring at $t = 2\,ns$). The result is given in Fig. 8, showing the integrated photon densities at the right and left cavities during and after this pulse excitation. It can be seen that before the pulse nearly no oscillations are present, while after the pulse anti-phase oscillations are visible. This is due to the fact that the 100 time traces before the pulse have a random phase, while the application of the pulse acts as a phase synchronizer. To better illustrate this concept, in the top-right inset two exemplary time traces for the left aperture are reported. These traces are part of the ensemble used for the averaging process. It can be seen how the PAB oscillations cancel out before the application of the pulse, while having the same phase after it.

We proceed with the experimental analysis of the pulse response. We employ the setup given in Fig. 9(a). The pulses are generated optically using an 810 nm Titanium:Sapphire laser (Ti:Sa). The light is coupled into a single mode fiber for beam shaping purposes. The fiber broadens the pulses to few ps pulse width. The pulse response of the VCSEL array is transmitted via a Bruker spectrometer toward a Hamamatsu streak camera, resulting in an actual temporal resolution of 9.3 ps. The spectrometer can be used in the typical first-order configuration to obtain spectral and temporal resolution in the streak camera or in the zeroth-order reflective configuration, resulting in spatial and temporal resolution. The

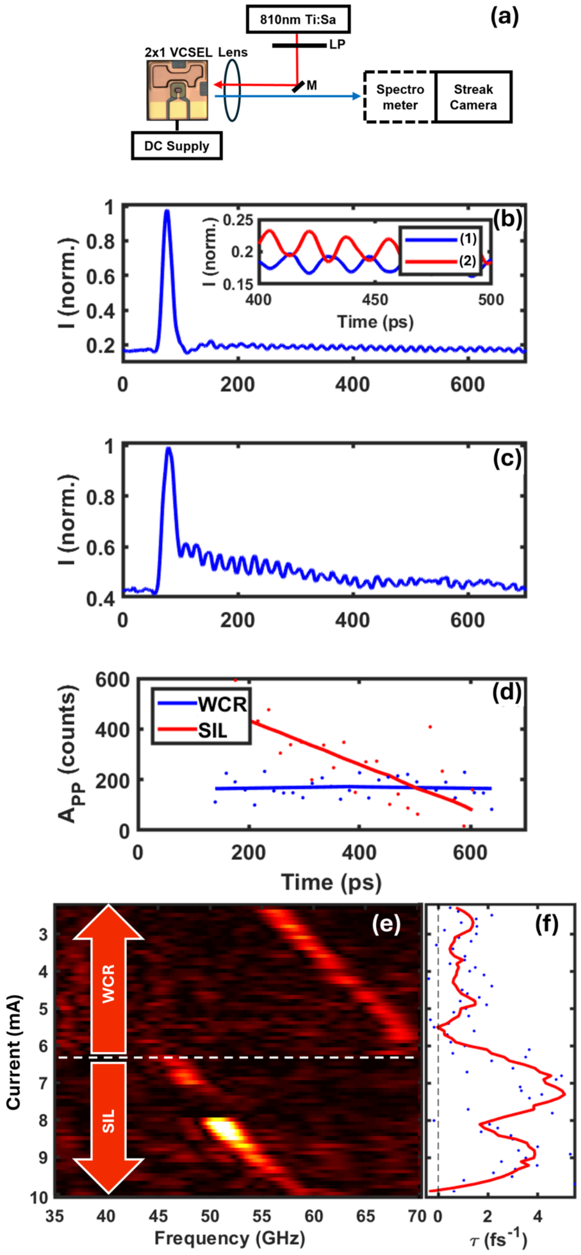

FIG. 9. (a) Experimental setup used for optical pulse injection. LP: Linear polarizer, Ti:Sa: Titanium:Sapphire laser, M: Mirror, OSA: Optical spectrum analyzer. (b) Pulse response of mode (1) intensity for 2.9 mA in the weakly coupled regime. The inset shows additionally the intensity of mode (2) with magnified axes ranges to point out that the oscillation is in anti-phase between the two modes. (c) Pulse response of mode (1)–(2) intensity for 8.2 mA in the self-injection locking regime. (d) Peak-to-peak amplitude over time extracted from the oscillations in (b) and (c). Dots show data points, solid lines are fits. (e) Fourier-transform of the response signals. (f) Damping constant of a $A(t) = A_0 \exp(-\tau t)$ fit of the oscillation amplitude in the response signals. Dots represent the data points, while the red line is a smoothed signal for better visualization.

working principle of the streak camera requires the Ti:Sa pulse as trigger event to start its fast acquisition.

Figure 9 shows the pulse response in the intensity I of mode (1) for the weakly coupled case at 2.9 mA (b) and of modes (1)–(2) in the self-injection locking case at 8.2 mA (c). The injection pulse takes place at approximately 80 ps and results in a significant initial peak in both cases. Afterward, the response continues with a fast oscillation which is not associated with the intensity dynamics resonance frequency but with the frequency separation of the fundamental supermodes, which we have shown in a previous publication.[27] In agreement with the simulations, the intensity of the two supermodes (1) and (2) oscillates with a phase shift of π, as depicted in the inset of Fig. 9(b), hindering recognition of the supermode interaction-related impulse responses in the overall intensity.

We analyze the peak-to-peak amplitude over time extracted from the data in Figs. 9(b) and 9(c) and plot it for comparison in Fig. 9(d). The solid lines are fits for improved visualization. It can be observed that the damping of the oscillation is very weak in the WCR case and the oscillation persists beyond the end of the measurement window used. In contrast, damping is significantly higher in the SIL case.

Figure 9(e) gives an overview of all the data collected during this measurement run; the frequency of the response oscillations depending on the bias current is shown and the two operational ranges are marked. The WCR ranges up to a value slightly higher than 6 mA, while the device operates in SIL for higher currents to the maximum current of 10 mA. It is visible that the response frequency tunes linearly with the current up to approximately 70 GHz at the transition from WCR to SIL operation. At this point, the response frequency has a discontinuity and starts to increase with current from approx. 47 GHz to approx. 60 GHz at the maximum current. In WCR, this frequency resembles the frequency difference of the two supermodes, while in SIL regime only one spectral peak is recognized [see Fig. 7(c)]. It can be observed that, in both simulations and experiments, the broad SIL feature has a lower center frequency than the narrow PAB peak. We attribute this to two main factors. First, while the PAB is approximately located at the frequency difference between the two lasing modes, our previous work[26] has shown that the PPR frequency undergoes a frequency correction arising from carrier interactions, which induce a chirp due to the non-zero linewidth enhancement factor. Furthermore, once the system transitions into the SIL regime, the frequency difference between the two cold-cavity modes can no longer be simply associated with the PPR frequency, since the lasing frequency is at an intermediate point of the cold cavity ones. For currents between 7 and 8 mA only a weak signal with few oscillations was observed, such that the signal gets only barely visible in the Fourier transform plot. This might be explained with the interaction with higher modes.

Figure 9(f) shows the damping constant τ evaluated from each response by fitting an exponential decay $A(t) = A_0 \cdot \exp(-\tau \cdot t)$ to the time dependent response oscillation amplitude $A(t)$ of the response oscillations. $A(t)$ has been extracted by finding all n oscillation minima $M_n(t_{M,n})$ and maxima $N_n(t_{N,n})$ and combining them to the oscillation amplitude $A((t_{M,n} + t_{N,n})/2) = |M_n + N_n|$. The plot reveals that the trend for very low damping in WCR operation and high damping in SIL operation described exemplary with Fig. 9(d) applies for the entire measured current range. This gives an indication that the WCR will not contribute to bandwidth enhancement but can be used for beat note generation, while the SIL regime, due to its higher damping, can act as bandwidth extension also for data transmission.

VI. ELECTRICAL MODULATION

The next part of our investigation is dedicated to continuous wave modulation. We begin with presentation and analysis of simulation results for the two regimes. In Fig. 10, the computed intensity modulation response is shown for three different currents. First, we report an example of WCR for 2 mA and an offset temperature of $T_{\mathrm{offset}} = 0\,\mathrm{K}$ from room temperature, computed using a sinusoidally modulated input signal and extracting the amplitude of the signal from the resulting response for each frequency step. Due to the PAB of the first two lasing modes, which feature a nonzero overlap, a very sharp peak is present in the IMR. This peak can be tuned via the bias current, as it will be demonstrated in the experiments later. Although detrimental for telecom devices, this can be utilized for applications such as optical carrier generation[17] or generation of terahertz radiation.[18]

The same analysis is done at 7.5 mA for an offset temperature of $T_{\mathrm{offset}} = 30\,\mathrm{K}$ from room temperature. Here, for the same reason, we observe a sharp PAB peak in the response. Furthermore, due to the greater coupling of the modes, also a broad feature is present, indicating an intermediate state between SIL and WCR.

Finally, the same simulation is repeated in the actual SIL regime for 8.0 mA. In this case, only a broader peak is present, yet providing a modest enhancement of the IMR. This latter regime is

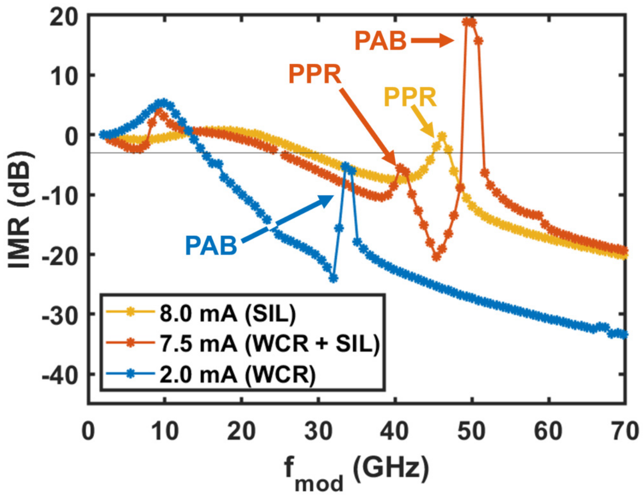

FIG. 10. Simulated intensity modulation response of a single aperture together with the -3 dB line for modulation frequencies f_{mod} up to 70 GHz. The response is reported at 2.0 mA (blue), featuring a PAB peak, 7.5 mA (red), presenting a PAB peak plus a broad PPR feature, and 8.0 mA (yellow), presenting solely a broad PPR feature.

suitable for datacom applications, since it provides an enhancement of the IMR without detrimental PAB oscillations.

We continue with the presentation of the experimental data. The experiment is performed with purely electrical modulation measurements without any optical injection. The measurement setup for electrical modulation using the streak camera is depicted in Fig. 11(a). We employ a sinusoidal modulation signal at a frequency range between modulation frequencies $f_{\mathrm{mod}} = 10\,\mathrm{GHz}$ and $f_{\mathrm{mod}} = 70\,\mathrm{GHz}$ (depicted up to 55 GHz), which is synchronized with the streak camera trigger signal. This enables periodic signals to be measured with very high bandwidth. We utilize modulation frequency step size of 151 MHz and extract the response amplitude from the temporal data for currents between 2 and 8 mA. The transmission of the RF components between signal generator and laser has been characterized with a vector network analyzer (VNA) for the entire frequency range and the resulting RF transmission variations were compensated.

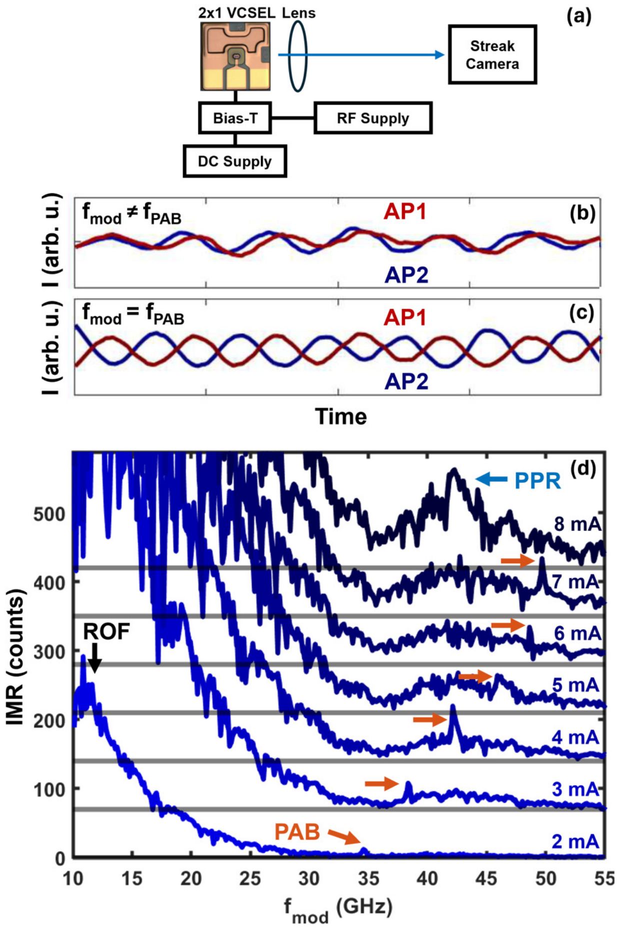

FIG. 11. Experimental setup used for electrical modulation measurements with a streak camera. The streak camera receives the trigger signal from the signal generator (a). Response signals in apertures 1 and 2 under electrical modulation; modulation frequency f_{mod} different from PAB frequency f_{PAB} (b), modulation frequency f_{mod} at PAB frequency f_{PAB} (c). Response amplitudes under electrical modulation measured with the streak camera (d). Each trace is shifted by 70 counts for better visualization. Gray lines mark the zero lines for each trace.

As a first step, exemplary traces for 7 mA are depicted for a modulation frequency at the PAB frequency in Fig. 11(b) and differing from the PAB frequency in Fig. 11(c). It can be observed that, comparable to the case under pulse excitation (see Fig. 9), the oscillation between the apertures is anti-phase for the resonance condition, while it is in phase for all other cases. Even though only a single modulation signal is applied to the entire laser array, the anti-phase oscillation between the apertures are observed.

From the amplitudes of the traces in Figs. 11(b) and 11(c), the response is calculated and depicted in Fig. 11(d). The plot reveals the ROF for the 2 mA trace around 12 GHz. Furthermore, up to 7 mA, a PAB peak can be found, increasing its frequency with current. This corresponds to the behavior expected from the pulse response measurement, in which the response frequency similarly increases with current. The difference between the PAB frequency under electrical modulation and the optical injection is attributed to differing temperature conditions due to the optical pumping pulses leading to additional heating.

For 8 mA, a broad PPR at a lower center frequency can be observed instead of a PAB peak, which is attributed to the SIL operation. The discontinuity of the center frequency and the enhanced resonance width caused by increased damping corresponds to the transition from the WCR to SIL range already observed in Fig. 9. This indicates that SIL can be useful for increased modulation bandwidth for data transfer.

When comparing the simulated responses in Fig. 10 with the experimental responses in Fig. 11(d), three aspects should be pointed out: First, as expected, the PAB frequency moves with bias current. Second, the transition between WCR and SIL, featuring both PAB and emerging broad PPR (orange trace in Fig. 10), can be also observed in the measurements. The emerging broad PPR is around 40–45 GHz and its maximum increases with increasing current. Third, the PAB peak amplitudes are much smaller than predicted by the simulations. The reason for this is attributed to the triggered nature of the streak camera based measurement technique: The PAB is considered to be always existing (as it is also proven by the fact PAB can be used for Terahertz generation without external modulation or excitation, as described in Ref. 18). However, the resulting oscillation's phase is not locked to the trigger signal of the streak camera, thus without synchronization of the free-running oscillation to the streak camera trigger, the PAB peak cannot be measured. While the optical pulse injection, due to the short nature of the pulse, induces a significant amount of carriers at a point in time well synchronized with the streak camera trigger signal, the modulation with a small electrical signal in the IMR measurement is not able to synchronize the free-running PAB to the streak camera trigger in the same extend as the pulse excitation. This results in a smaller PAB peak amplitude due to the averaging nature of the streak camera measurement for signals with low synchronization to the trigger.

To prove this, we perform an IMR measurement using an untriggered method using a VNA as depicted in the setup sketch in

Fig. 12(a). For this experiment, we use a different sample with a lower PAB frequency range in order to stay below the limitations of the equipment of $< 40\,\mathrm{GHz}$. The light of each aperture is coupled into a single mode fiber consecutively and the S21 frequency response is measured with the VNA. The two response curves are depicted in Fig. 12(b). Both show a relaxation oscillation frequency around 8 GHz. It is furthermore possible to observe a PAB peak at 22.5 GHz with significant amplitude, comparable to the simulations. This strongly supports our assumption that the reduced peak amplitudes in Fig. 11 are caused by the triggered nature of the measurement method. Using the VNA, it was only possible to observe the WCR, as SIL occurs at higher currents leading to higher PPR frequencies outside the measurement range of the VNR.

All three regimes observed in the dynamical analysis based on simulations are qualitatively observed in the experiments as well. Still, quantitative differences between simulations and experimental data can be seen. A precise and more quantitative fitting of the IMR at each current would require a self consistent thermal and electromagnetic solution due to the sensitivity of modal features to this latter aspect. This however goes beyond the scope of this work, and would require a much more complex multiphysics approach.[37]

Finally, using the setup in Fig. 12(a) we also measure the transmission of a non-return-to-zero pseudo random bit sequence of the sample operated at 8 mA in the SIL regime, without pre-emphasis at the driver and equalization at the receiver side. The measured eye diagram with a significant opening is depicted in Fig. 12(c). This shows that PAB which appears in the WCR does neither degrade large signal modulation nor eye opening of the laser. Instead, under operation in the SIL regime, the bit error rate can be reduced to $BER < 10^{-25}$.

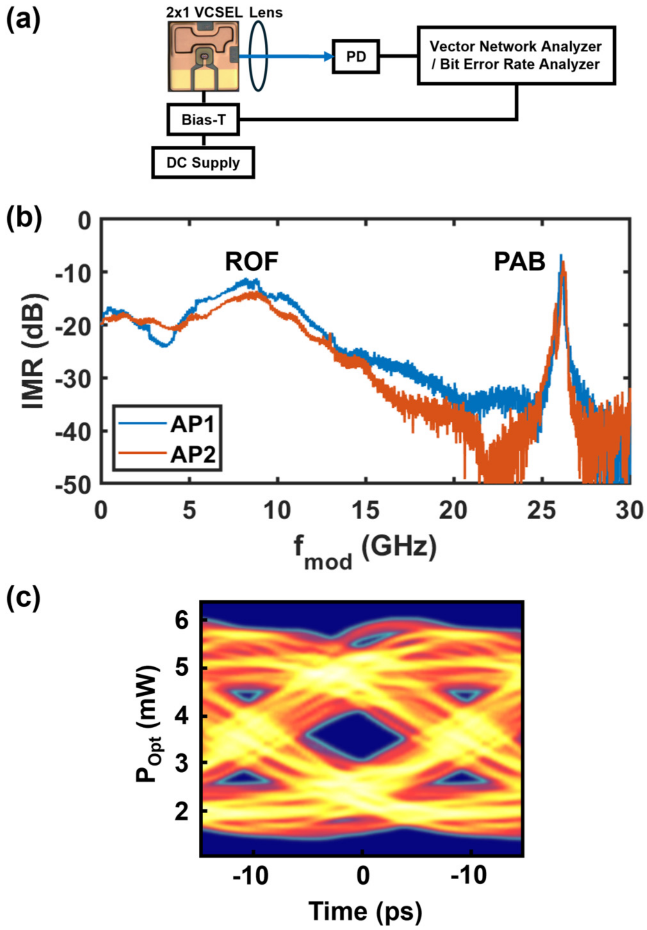

FIG. 12. (a) Measurement setup (PD: Photo diode). Vector network analyzer is used to measure the modulation response for each aperture with a single mode fiber. (b) Modulation response at bias of 1.5 mA with ROF and PAB frequency marked. (c) Eye diagram of a random bit sequence transmission in SIL operation measured using a Bit Error Rate Analyzer.

VII. CONCLUSION

In this study, we provide and extensive investigation and understanding on laterally coupled vertical-cavity surface-emitting laser structures with a single common electrical contact being operated in both weakly coupled range and demonstrated for the first time, a strongly coupled, self-injection locked range, enabling fundamentally different operational regimes. The weak coupling enables narrow tunable plasma-assisted beating peaks with current-dependent wide frequency tuning range. Strong coupling adds a broader resonance to the modulation dynamics, enabling extension of the modulation bandwidth. Switching between the two regimes of operation is possible via bias current. Excellent agreement between experiments and simulations is found and enables comprehensive understanding of the dynamics of supermodes in our oxide-confined single-contact coupled-cavity VCSELs. The standard fabrication process and the simplicity of operation as well as the demonstrated coherent operation enables a more cost-effective and easy-to-use technology and expands the potential of TCCs for industrial applications.

The device under investigation with an almost perfect cavity symmetry shows a small improvement in intensity modulation response in the self-injection locked regime. Theoretical investigations point out a path toward future improved device structure.[26] They predict zero performance improvement for perfectly symmetric structures, while increased performance is obtained for devices using cavities with symmetry-breaking.

Furthermore, a novel effect of anti-phase intensity modulation under single-phase high-frequency external electrical excitation was found. This effect in combination with tuning of the resonance frequency by current deserves further study, as it may enable new applications in sensing, optical synchronization, and coherent data transmission by allowing precise matching of the reference input frequency and the single-phase high-quality HF-modulated optical signal at the same frequency by monitoring the phase difference and/or the modulation intensity of the light emitted by each of the coupled apertures.

Besides optical data transmission links with extended bandwidth, also other applications like radio-over-fiber,[17] generation of THz radiation[18] and beam-steering applications[19,20] can be addressed utilizing our mini-array VCSELs.

ACKNOWLEDGMENTS

This research was funded by Bundesministerium fúr Bildung und Forschung within the EUROSTARS project "COHORT" (No. 01QE2432B). The sole responsibility for the content of this publication lies with the authors. We thank the German Research Foundation (DFG) for funding within the Reinhart-Koselleck-Project No. 490699635.

AUTHOR DECLARATIONS

Conflict of Interest

The authors have no conflicts to disclose.

Author Contributions

M. Lindemann: Conceptualization (lead); Data curation (lead); Formal analysis (lead); Funding acquisition (equal); Investigation (lead); Methodology (equal); Project administration (equal); Supervision (equal); Validation (equal); Visualization (lead); Writing – original draft (lead); Writing – review & editing (equal). **M. D'Alessandro:** Formal analysis (equal); Investigation (equal); Methodology (equal); Software (lead); Validation (equal); Visualization (equal); Writing – original draft (equal); Writing – review & editing (equal). **N. Ledentsov Jr.:** Conceptualization (equal); Funding acquisition (equal); Investigation (equal); Resources (equal); Visualization (equal); Writing – review & editing (equal). **O. Y. Makarov:** Resources (equal); Writing – review & editing (equal). **N. N. Ledentsov:** Conceptualization (equal); Funding acquisition (equal); Resources (equal); Writing – review & editing (equal). **A. Tibaldi:** Conceptualization (equal); Funding acquisition (equal); Resources (equal); Writing – review & editing (equal). **N. C. Gerhardt:** Funding acquisition (equal); Writing – review & editing (equal). **M. R. Hofmann:** Funding acquisition (equal); Resources (equal); Supervision (equal); Writing – review & editing (equal).

DATA AVAILABILITY

The data that support the findings of this study are available from the corresponding author upon reasonable request.

REFERENCES

[1] J. Hecht, "The bandwidth bottleneck that is throttling the internet," Nature **536**, 139–142 (2016).

[2] N. Jones, "How to stop data centres from gobbling up the world's electricity," Nature **561**, 163–166 (2018).

[3] A. Paraskevopoulos *et al.*, "Ultra-high-bandwidth (> 35 GHz) electro-optically-modulated VCSEL," in *Proceedings of the Optical Fiber Communication Conference and National Fiber Optic Engineers Conference* (IEEE, 2006), pp. 1–3.

[4] V. A. Shchukin *et al.*, "Digital data transmission using electro-optically modulated vertical-cavity surface-emitting laser with saturable absorber," Appl. Phys. Lett. **104**, 051125 (2014).

[5] M. Tan, S. Fryslie, J. Lott, N. Ledentsov, D. Bimberg, and K. Choquette, "Error-free transmission over 1-km OM4 multimode fiber at 25 Gb/s using a single mode photonic crystal vertical-cavity surface-emitting laser," IEEE Photon. Technol. Lett. **25**, 1823–1825 (2013).

[6] M. Lindemann *et al.*, "Ultrafast spin-lasers," Nature **568**, 212 (2019).

[7] B. Tromborg *et al.*, "Transmission line description of optical feedback and injection locking for Fabry Perot and DFB lasers," IEEE J. Quantum Electron. **23**, 1875–1889 (1987).

[8] H. Dalir and F. Koyama, "29 GHz directly modulated 980 nm vertical-cavity surface emitting lasers with bow-tie shape transverse coupled cavity," Appl. Phys. Lett. **103**, 091109 (2013).

[9] S. T. M. Fryslie, M. P. T. Siriani, D. F. Siriani, M. T. Johnson, and K. D. Choquette, "37-GHz modulation via resonance tuning in single-mode coherent vertical-cavity laser arrays," IEEE Photon. Technol. Lett. **27**, 415–418 (2015).

[10] D. F. Siriani and K. D. Choquette, "Coherent coupling of vertical-cavity surface-emitting laser arrays," in *Advances in Semiconductor Lasers, Semiconductors and Semimetals Series*, Vol. 86, edited by J. J. Coleman, A. C. Bryce, and C. Jagadish (Elsevier, Amsterdam, 2012), Chap. 6, pp. 227–267.

[11] S. T. M. Fryslie *et al.*, "Modulation of coherently coupled phased photonic crystal vertical cavity laser arrays," IEEE J. Sel. Top. Quantum Electron. **23**, 1–9 (2017).

[12] W. North, N. Jahan, P. Strzebonski, A. Khurana, S. E. Ralph, and K. D. Choquette, "Analysis and characterization of photon–photon resonance in coupled dual-element photonic crystal vertical cavity surface emitting laser arrays," J. Lightwave Technol. **42**, 236–242 (2024).

[13] H. R. Ibrahim, A. Hassan, X. Gu, and F. Koyama, "Enhanced high-frequency modulation of single-mode 850 nm VCSELs via dual transverse-cavity integration," IEICE Electronics Express **21**, 1–4 (2024).

[14] E. Heidari, H. Dalir, M. Ahmed, V. J. Sorger, and R. T. Chen, "Hexagonal transverse-coupled-cavity VCSEL redefining the high-speed lasers," Nanophotonics **9**, 4743–4748 (2020).

[15] H. Dave *et al.*, "Digital modulation of coherently-coupled 2 × 1 vertical-cavity surface-emitting laser arrays," IEEE Photon. Technol. Lett. **31**, 173–176 (2019).

[16] M. Tornatore, G.-K. Chang, and G. Ellinas eds., *Fiber-Wireless Convergence in Next-Generation Communication Networks: Systems, Architectures, and Management* (Springer, 2017).

[17] H. Dalir, A. Matsutani, M. Ahmed, A. Bakry, and F. Koyama, "High frequency modulation of transverse-coupled-Cavity VCSELs for radio over fiber applications," IEEE Photon. Technol. Lett. **26**, 281–283 (2014).

[18] Y. Hu, C. Brenner, M. R. Hofmann, and M. Lindemann, "Coherent CW THz generation with a coupled-cavity mini-array VCSEL," Electron. Lett. **61**, e70146 (2025).

[19] K. Choquette, J. Raftery, and A. Lehman, "Beam steering in photonic crystal vertical cavity semiconductor laser arrays," in *2006 IEEE Aerospace Conference* (IEEE, 2006), p. 7.

[20] G. Pan, C. Xu, Y. Xie, Y. Dong, Q. Wang, J. Deng, J. Sun, and H. Chen, "Ultra-compact electrically controlled beam steering chip based on coherently coupled VCSEL array directly integrated with optical phased array," Opt. Express **27**, 13910–13922 (2019).

[21] E. Kapon, J. Katz, and A. Yariv, "Supermode analysis of phase-locked arrays of semiconductor lasers," Opt. Lett. **9**, 125–127 (1984).

[22] W. J. Fader and G. E. Palma, "Normal modes of n coupled lasers," Opt. Lett. **10**, 381–383 (1985).

[23] W. W. Chow, "Effects of spatial gain variation in an index-guided semiconductor laser array," J. Opt. Soc. Am. B **4**, 324–328 (1987).

[24] M.-A. Miri and A. Alú, "Exceptional points in optics and photonics," Science **363**, eaar7709 (2019).

[25] Z. Gao, S. T. M. Fryslie, B. J. Thompson, P. S. Carney, and K. D. Choquette, "Parity-time symmetry in coherently coupled vertical cavity laser arrays," Optica **4**, 323–329 (2017).

[26] M. D'Alessandro, V. Torrelli, F. Bertazzi, M. Goano, N. N. Ledentsov, M. Lindemann, M. Gioannini, P. Debernardi, and A. Tibaldi, "Transverse coupled cavity VCSELs: Bridging ultrabroadband dynamics to optical supermodes," IEEE Photon. J. **16**, 1–7 (2024).

[27] M. Lindemann, N. C. Gerhardt, M. Hofmann, N. J. Ledentsov, V. A. Shchukin, N. N. Ledentsov, O. Y. Makarov, Ł. Chorchos, and

J. P. Turkiewicz, "Coupled aperture VCSELs suitable for 100 GHz intensity modulation," in *2023 23rd International Conference on Transparent Optical Networks (ICTON)* (IEEE, 2023).

[28] M. Yousefi and D. Lenstra, "Rate-equation description of multi-mode semiconductor lasers," Proc. SPIE **8980**, 89800B (2014).

[29] P. Debernardi, "Hot-VELM: A comprehensive and efficient code for fully vectorial and 3-D hot-cavity VCSEL simulation," IEEE J. Quantum Electron. **45**, 979–992 (2009).

[30] A. Gullino *et al.*, "AlGaAs tunnel junction (tj)-VCSELs: A NEGF–drift-diffusion approach," IEEE Photon. J. **16**, 1–9 (2024).

[31] N. Ledentsov Jr., V. A. Shchukin, L. Chorchos, O. Y. Makarov, J.-R. Kropp, I. E. Titkov, V. P. Kalosha, V. Zerova, M. Lindemann, N. C. Gerhardt, M. D'Alessandro, V. Torrelli, P. Debernardi, A. Tibaldi, M. R. Hofmann, and N. N. Ledentsov, "Analysis of laterally-coupled-cavity VCSELs for ultra-high-frequency photon–photon resonance modulation," in *Proceedings of SPIE OPTO, Vertical-Cavity Surface-Emitting Lasers XXVIII*, Vol. 12904 (Published by SPIE, 2024), p. 1290405.

[32] C. Geuzaine and J.-F. Remacle, "Gmsh: A 3-D finite element mesh generator with built-in pre- and post-processing facilities," Int. J. Numer. Methods Eng. **79**, 1309–1331 (2009).

[33] The MathWorks Inc, see https://it.mathworks.com/help/matlab/ref/ode45.html for "MATLAB ODE45 Routine."

[34] C.-H. Chang, L. Chrostowski, and C. Chang-Hasnain, "Injection locking of VCSELs," IEEE J. Sel. Top. Quantum Electron. **9**, 1386–1393 (2003).

[35] S. M. Misak, "Spectrally resolved imaging of the transverse modes in multi-mode VCSELs," in *Proceedings of SPIE 19th Vertical-Cavity Surface-Emitting Lasers* (Published by SPIE, 2015), p. 93810L.

[36] S. T. M. Fryslie, M. T. Johnson, and K. D. Choquette, "Coherence tuning in optically coupled phased vertical cavity laser arrays," IEEE J. Quantum Electron. **51**, 2600206 (2015).

[37] A. Tibaldi, F. Bertazzi, M. Goano, R. Michalzik, and P. Debernardi, "VENUS: A vertical-cavity surface-emitting laser electro-opto-Thermal NUmerical simulator," IEEE J. Sel. Top. Quantum Electron. **25**, 1–12 (2019).